Supplementary Information

Influence of the substituents of thiol ligand on the optical properties of $AuCu_{14}$

Yu-Jing Zhao,‡[a] Jin-Sen Yang,‡[ab], Jing Li,[c] Yu-Bing Si,[a] Lu-Yao Xiao,[a] Zhao-Yang Wang,[a] Jia-Hua Hu,*[a] Xi-Yan Dong[ab] and Shuang-Quan Zang[a]

*Correspondence: jhhu@zzu.edu.cn (J.-H. Hu)

Experimental Details

Reagents and Materials Used. All chemicals and solvents obtained from suppliers were used without further purification, including hydrogen tetrachloroaurate ($HAuCl_4$•$4H_2O$, 99.9%), tetraoctylammonium bromide (TOAB, 95%), triphenylphosphine (PPh_3, 98%), cuprous chloride (CuCl, 99.9%), 4-tert-butylthiophenol ($C_{10}H_{14}S$, TBBT, 98%), sodium borohydride ($NaBH_4$, 99.9%), sodium hexafluoroantimonate ($NaSbF_6$, 99%), fluorothiophenol (HSC_6H_4F, 98%), bis(triphenylphosphine)copper tetrahydroborate ($(PPh_3)_2CuBH_4$, 98%), 4-triethylamine (NEt_3, 99%), dichloromethane (CH_2Cl_2, A.R.), methanol (CH_3OH, A.R.), acetone (C_3H_6O, A.R.) and ether ($C_4H_{10}O$, A.R.).

Materials Preparation. Synthesis of **$AuCu_{14}$-F** and **$AuCu_{14}$-$C(CH_3)_3$**. The synthesis of two $AuCu_{14}$ clusters followed the procedures reported previously.[1, 2] Elemental analysis (%) for evacuated **$AuCu_{14}$-F** ($C_{180}H_{138}AuCu_{14}P_6S_{12}F_{18}Sb$): calcd. C 48.89, H 3.15, S 8.70; found C 48.76, H 3.18, S 8.26. Elemental analysis (%) for evacuated **$AuCu_{14}$-$C(CH_3)_3$** ($C_{228}H_{246}AuCu_{14}P_6S_{12}F_6Sb$): calcd. C 56.12, H 5.08, S 7.89; found C 57.12, H 5.15, S 7.72.

Material Characterizations. Powder X-ray diffraction (PXRD) patterns of **$AuCu_{14}$-F** and **$AuCu_{14}$-$C(CH_3)_3$** were collected at room temperature in air using an X'Pert PRO diffractometer (Cu-Kα). Fourier transform infrared (FT-IR) spectra were recorded on a Bruker TENSOR 27 FT-IR spectrometer in the 400-4000 cm^{-1} region with KBr pellets. Thermogravimetry analyses (TGA) were performed on a TA Q50 system under an N_2 atmosphere (flow rate = 60 $mL \cdot min^{-1}$) in the temperature range 30-500 °C at a heating rate of 10 °C min^{-1}. Mass spectra (MS) were recorded on an X500R QTOF spectrometer. Elemental analyses (EA) were carried out with a Perkin-Elmer 240 elemental analyzer. UV-vis absorption spectra were recorded using a Hitachi UH4150 UV-Visible spectrophotometer in the range 350-800 nm. UV-visible diffuse reflectance spectra of samples were recorded at room temperature in the range of 280-1200 nm using a UH4150 spectrophotometer equipped with an integrating sphere. The room temperature steady-state spectroscopy, time-resolved photoluminescence (PL),

temperature-dependent emission spectra and photoluminescence quantum yield were measured on the HORIBA FluoroLog-3 fluorescence spectrometer.

DFT calculation. The density functional theory (DFT) and time-dependent density functional theory (TD-DFT) calculations were performed with Gaussian 16.[3] The geometric optimization of the ground state calculations was performed under PBE0 functional and using 6-31g* basis set for H, C, S, P, and F atoms and Lanl2DZ effective core potentials for Au and Cu atoms. Well-converged geometries are obtained by tightening the energy and gradient convergence criteria to 1×10^{-6} Hartree and 1×10^{-3} Hartree/Å, respectively. The theoretical UV-Vis spectra of **$AuCu_{14}$-F** and **$AuCu_{14}$-$C(CH_3)_3$** were calculated using TD-DFT and plotted based on the computation of the lowest 300 singlet-to-singlet excitation energies. The SMD solvent model (dichloromethane) was applied in all calculations.

Transient absorption (TA) measurement. The transient absorption spectra were recorded on a commercial pump-probe system with microscope (Helios-EOS, Ultrafast Systems LLC) in combination with a femtosecond laser system (Astrella, Coherent). Laser pulses (800 nm center wavelength, 100 fs duration, 1 kHz repetition rate, 7 mJ/pulse) were generated by a Ti:Sapphire-based regenerative amplified laser system. The laser pulses were spilt to generate pump and probe beam. The pump pulses at 400 nm were delivered by an optical parametric amplifier which was excited by a portion of 800 nm laser pulses. For femtosecond transient absorptions in DCM solution, the pump pulse energy in each measurement was 25 μJ/cm^2 at the sample cell. The probe and reference beams were generated by focusing the 800 nm beam (split from the amplifier with a tiny portion) to a sapphire crystal. The pump-probe delay was controlled by an optical delay line. For the nanosecond transient absorptions in DCM solution, the probe and reference beams were provided by an additional supercontinuum laser (370-900 nm, 0.5 ns duration, 2 kHz repetition rate). The pump-probe delay time was electronically controlled. TA signal was obtained by detecting the intensity of probe and reference pulses with and without pumped light, and global analysis was performed by Glotaran software.

Femtosecond transient absorptions of $AuCu_{14}$ crystal are measured by the single crystal microimaging detection system, and the specific position of a single crystal is measured by a long working distance 50× objective lens. The camera provides a direct enlarged view of the sample. The probe beam was generated by focusing the 800 nm beam to another sapphire crystal. The pump pulse energy in each measurement was 250 $\mu J/cm^2$ at the crystal. The pump-probe delay also was controlled by the same optical delay line. TA signal is obtained by detecting the intensity of probe light with and without pumped light, and global analysis is performed by Glotaran software.

Supplementary Figures S1-S20

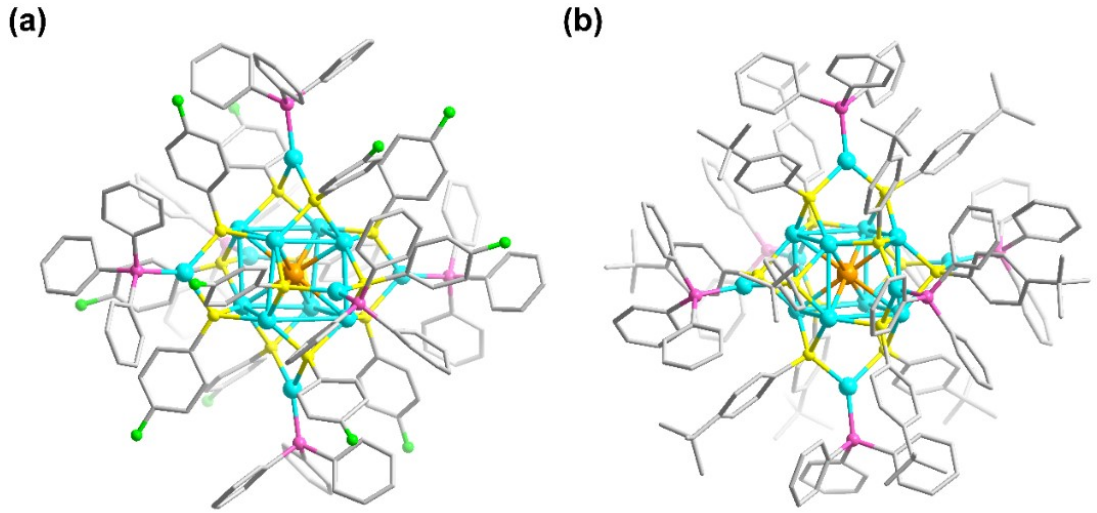

Fig. S1. Overall structure of (a) **$AuCu_{14}$-F** and (b) **$AuCu_{14}$-$C(CH_3)_3$** crystal. Orange: Au, cyan: Cu, yellow: S, pink: P, gray: C, green: F. All hydrogen atoms have been omitted for clarity.

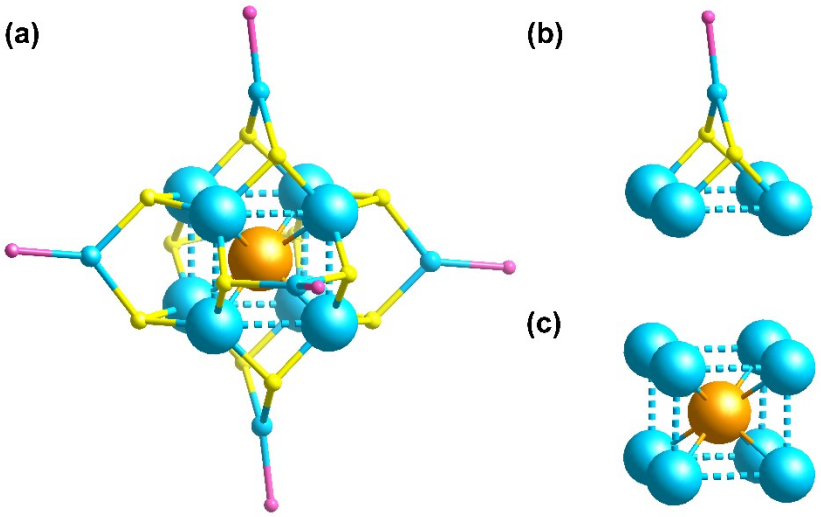

Fig. S2. Local structure of $AuCu_{14}$ cluster. (a) the surface motif of Cu-S and Cu-P. (b) the $(SR)_2CuPPh_3$ mount motif capping on the square face of the Cu_8 shell. (c) the body-centered cubic $AuCu_8$. Orange: Au, cyan: Cu, yellow: S, pink: P, gray: C, green: F. All hydrogen atoms have been omitted for clarity.

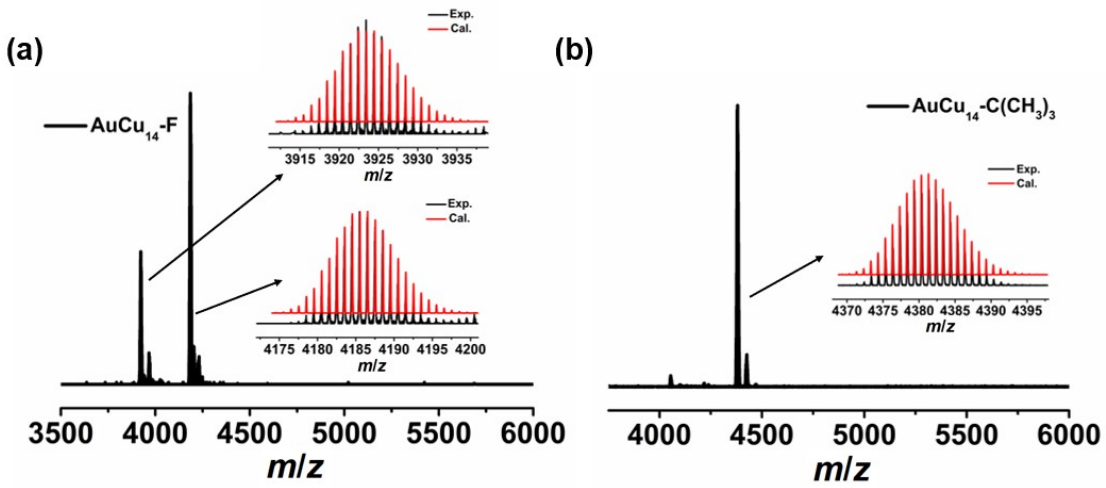

Fig. S3. Positive mode ESI-MS of (a) **$AuCu_{14}$-F** and (b) **$AuCu_{14}$-$C(CH_3)_3$** in DCM. **$AuCu_{14}$-F** showed two prominent peaks at *m/z* 4186.50 Da and 3923.41 Da, of which one corresponded to monoca-tionic $[AuCu_{14}(SC_6H_4\text{-}R)_{12}(PPh_3)_5]^+$, (R=F, calcd *m/z* 4186.56 Da) and the other to $[AuCu_{14}(SC_6H_4\text{-}R)_{12}(PPh_3)_6]^+$ (R=F, calcd *m/z* 3923.47 Da), respectively; **$AuCu_{14}$-$C(CH_3)_3$** only showed a prominent peak at *m/z* 4381.39 Da where it corresponded to monoca-tionic $[AuCu_{14}(SC_6H_4\text{-}R)_{12}(PPh_3)_5]^+$, (R=$C(CH_3)_3$, calcd *m/z* 4381.33 Da).

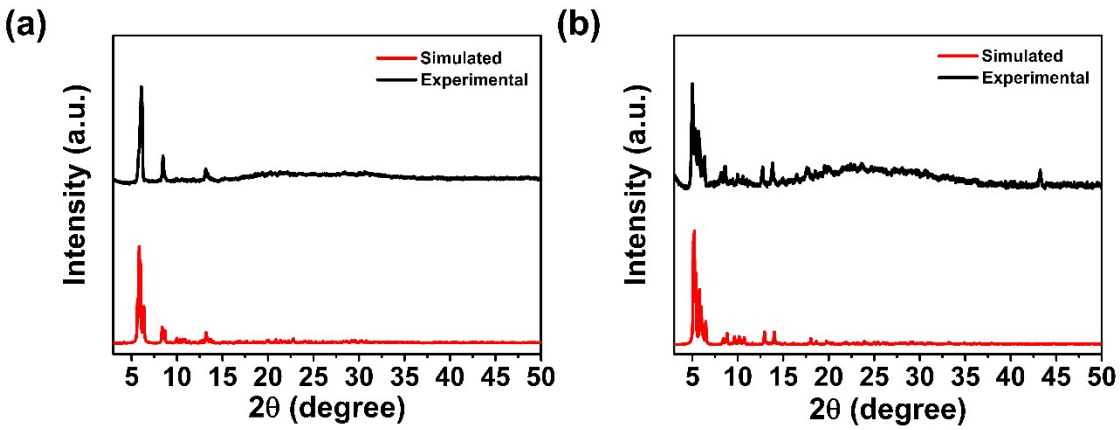

Fig. S4. The experimental and simulated PXRD spectra of (a) **$AuCu_{14}$-F** and (b) **$AuCu_{14}$-$C(CH_3)_3$**.

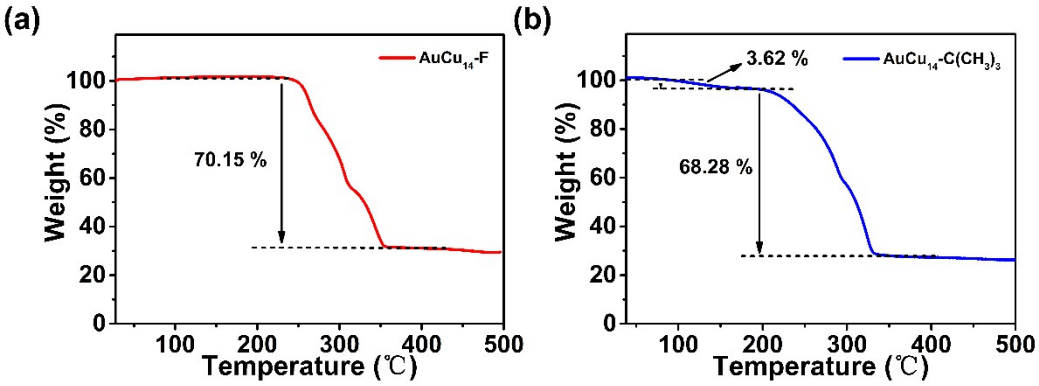

Fig. S5. The thermal gravimetric curve of (a) **$AuCu_{14}$-F** and (b) **$AuCu_{14}$-$C(CH_3)_3$**. **$AuCu_{14}$-F**: The weight loss (70.15%) between 230 ˚C and 365 ˚C should be caused by the ligands complete dissociation (calcd 70.10%). **$AuCu_{14}$-$C(CH_3)_3$**: The first weight loss (3.62%) from 90 ˚C to 180 ˚C could be ascribed to the removal of one -SC_6H_4-$C(CH_3)_3$ (calcd 3.39%), and the weight loss (68.28%) between 200 ˚C and 340 ˚C should be caused by the ligands complete dissociation (calcd 69.51%).

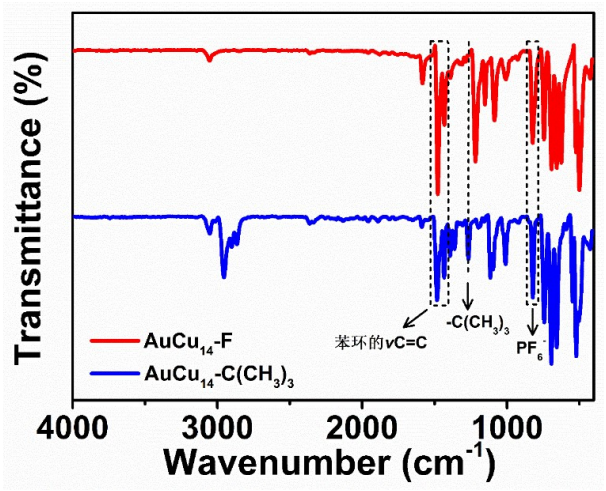

Fig. S6. FT-IR spectra of **$AuCu_{14}$-F** and **$AuCu_{14}$-$C(CH_3)_3$**.

Tab. S1. Hirshfeld percentage of orbital compositions of frontier molecular orbitals in SC_6H_4-F and SC_6H_4-$C(CH_3)_3$. S refers to the sulfur atom, C_6H_4-R refer to the atoms of C_6H_4-R groups (R=F or $C(CH_3)_3$).

		S	C_6H_4-R
Compound	Orb#	Composition	Composition
SC_6H_4-F	HOMO	41.33%	58.67%
	LUMO	1.60%	98.40%
SC_6H_4-$C(CH_3)_3$	HOMO	40.26%	59.74%
	LUMO	2.38%	97.62%

Tab. S2. The Hirshfeld charge of single metal atom and the average Hirshfeld charge in each layer based on optimized geometry of SC_6H_4-F and SC_6H_4-$C(CH_3)_3$. S refers to the sulfur atom, Ph refers to benzene ring and -R refers to -F or -$C(CH_3)_3$, respectively.

SC_6H_4-F		SC_6H_4-$C(CH_3)_3$			
Atom	Hirshfeld Charge (e)	Atom	Hirshfeld Charge (e)	Atom	Hirshfeld Charge (e)
C1	0.087	C1	-0.000	C14	-0.092
C2	-0.053	C2	-0.041	H15	0.030
C3	-0.044	C3	-0.054	H16	0.031
C4	-0.019	C4	-0.017	H17	0.033
C5	-0.046	C5	-0.054	C18	-0.092
C6	-0.054	C6	-0.044	H19	0.033
H7	0.056	H7	0.043	H20	0.032
H8	0.051	H8	0.042	H21	0.032
H9	0.047	H9	0.045	C22	-0.092
H10	0.056	H10	0.042	H23	0.033
S11	-0.043	S11	-0.048	H24	0.031
H12	0.061	H12	0.059	H25	0.030
F13	-0.100	C13	0.019		

Average Hirshfeld Charge (e)			
	S	Ph	-R
-F	-0.043	0.081	-0.100
-$C(CH_3)_3$	-0.048	-0.038	0.028

Tab. S3. The primary bond length of **AuCu$_{14}$-F**.

Bond	Length (Å)	Bond	Length (Å)
Au1-Cu3	2.7947(17)	Au1-Cu4	2.6563(16)
Au1-Cu5	2.7464(15)	Au1-Cu7	2.6448(20)
Au1-Cu10	2.7947(17)	Au1-Cu11	2.6563(16)
Au1-Cu12	2.7464(15)	Au1-Cu14	2.6448(20)
Cu3-Cu4	3.0635(23)	Cu3-Cu5	3.2748(23)
Cu3-Cu7	3.2188(27)	Cu4-Cu12	3.2147(23)
Cu4-Cu14	2.8633(23)	Cu5-Cu11	3.2147(23)
Cu5-Cu14	3.1597(27)	Cu7-Cu11	2.8633(23)
Cu7-Cu12	3.1597(27)	Cu10-Cu11	3.0635(23)
Cu10-Cu12	3.2748(23)	Cu10-Cu14	3.2188(27)
Cu3-S1	2.2875(30)	Cu3-S4	2.2682(33)
Cu3-S5	2.2619(29)	Cu4-S2	2.3063(31)
Cu4-S5	2.2873(30)	Cu4-S9	2.2979(27)
Cu5-S1	2.282(3)	Cu5-S3	2.2869(32)
Cu5-S12	2.2858(34)	Cu7-S4	2.2764(32)
Cu7-S6	2.3319(33)	Cu7-S8	2.2610(35)
Cu10-S7	2.2875(30)	Cu10-S10	2.2682(33)
Cu10-S11	2.2619(29)	Cu11-S3	2.2979(27)
Cu11-S8	2.3063(31)	Cu11-S11	2.2873(30)
Cu12-S6	2.2858(34)	Cu12-S7	2.282(3)
Cu12-S9	2.2869(32)	Cu14-S2	2.2610(35)
Cu14-S10	2.2764(32)	Cu14-S12	2.3319(33)
S1-Cu2	2.2716(30)	S2-Cu2	2.269(3)
S3-Cu1	2.2629(29)	S4-Cu1	2.2726(28)
S5-Cu6	2.2612(28)	S6-Cu6	2.2736(33)
S7-Cu9	2.2716(30)	S8-Cu9	2.269(3)
S9-Cu8	2.2629(29)	S10-Cu8	2.2726(28)
S11-Cu13	2.2612(28)	S12-Cu13	2.2736(33)

Tab. S4. The primary bond length of **$AuCu_{14}$-$C(CH_3)_3$**.

Bond	Length (Å)	Bond	Length (Å)
Au1-Cu2	2.7227(11)	Au1-Cu4	2.7133(10)
Au1-Cu5	2.7528(11)	Au1-Cu6	2.5766(10)
Au1-Cu9	2.7227(11)	Au1-Cu11	2.7134(10)
Au1-Cu12	2.7527(11)	Au1-Cu13	2.5767(10)
Cu2-Cu4	3.1309(13)	Cu2-Cu5	3.3160(14)
Cu2-Cu6	3.0385(23)	Cu4-Cu12	3.1911(23)
Cu4-Cu13	3.0590(15)	Cu5-Cu11	3.1911(23)
Cu5-Cu13	2.9236(13)	Cu6-Cu11	3.0590(15)
Cu6-Cu12	2.9236(13)	Cu9-Cu11	3.1309(13)
Cu9-Cu12	3.3160(14)	Cu9-Cu13	3.0385(23)
Cu2-S4	2.2823(17)	Cu2-S5	2.2947(26)
Cu2-S6	2.2709(21)	Cu4-S1	2.2925(21)
Cu4-S5	2.2865(27)	Cu4-S8	2.2702(18)
Cu5-S3	2.2691(25)	Cu5-S4	2.3063(18)
Cu5-S7	2.2737(30)	Cu6-S2	2.2745(19)
Cu6-S6	2.2815(28)	Cu6-S9	2.2815(26)
Cu9-S10	2.2823(17)	Cu9-S11	2.2947(26)
Cu9-S12	2.2709(21)	Cu11-S2	2.2702(18)
Cu11-S7	2.2925(21)	Cu11-S11	2.2865(27)
Cu12-S1	2.2737(30)	Cu12-S9	2.2691(25)
Cu12-S10	2.3063(18)	Cu13-S3	2.2815(26)
Cu13-S8	2.2745(19)	Cu13-S12	2.2815(28)
S1-Cu1	2.2629(19)	S2-Cu3	2.2438(27)
S3-Cu7	2.2498(28)	S4-Cu3	2.2535(24)
S5-Cu7	2.2403(21)	S6-Cu1	2.2429(18)
S7-Cu8	2.2629(19)	S8-Cu10	2.2438(27)
S9-Cu14	2.2498(28)	S10-Cu10	2.2535(24)
S11-Cu14	2.2403(21)	S12-Cu8	2.2429(18)

Tab. S5. Average bond lengths (Å) in **$AuCu_{14}$-F** and **$AuCu_{14}$-$C(CH_3)_3$**.

	Au-Cu	Cu-Cu	Cu-S
$AuCu_{14}$-F	2.711	3.133	2.280
$AuCu_{14}$-$C(CH_3)_3$	2.692	3.109	2.271

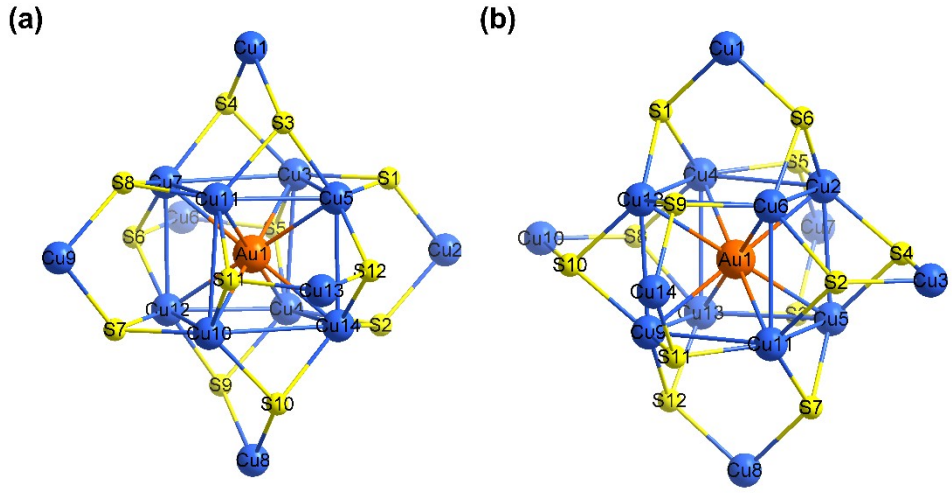

Fig. S7. The Hirshfeld charge analyses on (a) **$AuCu_{14}$-F** and (b) **$AuCu_{14}$-$C(CH_3)_3$**. Orange: Au, blue: Cu, yellow: S. Other atoms have been omitted for clarity.

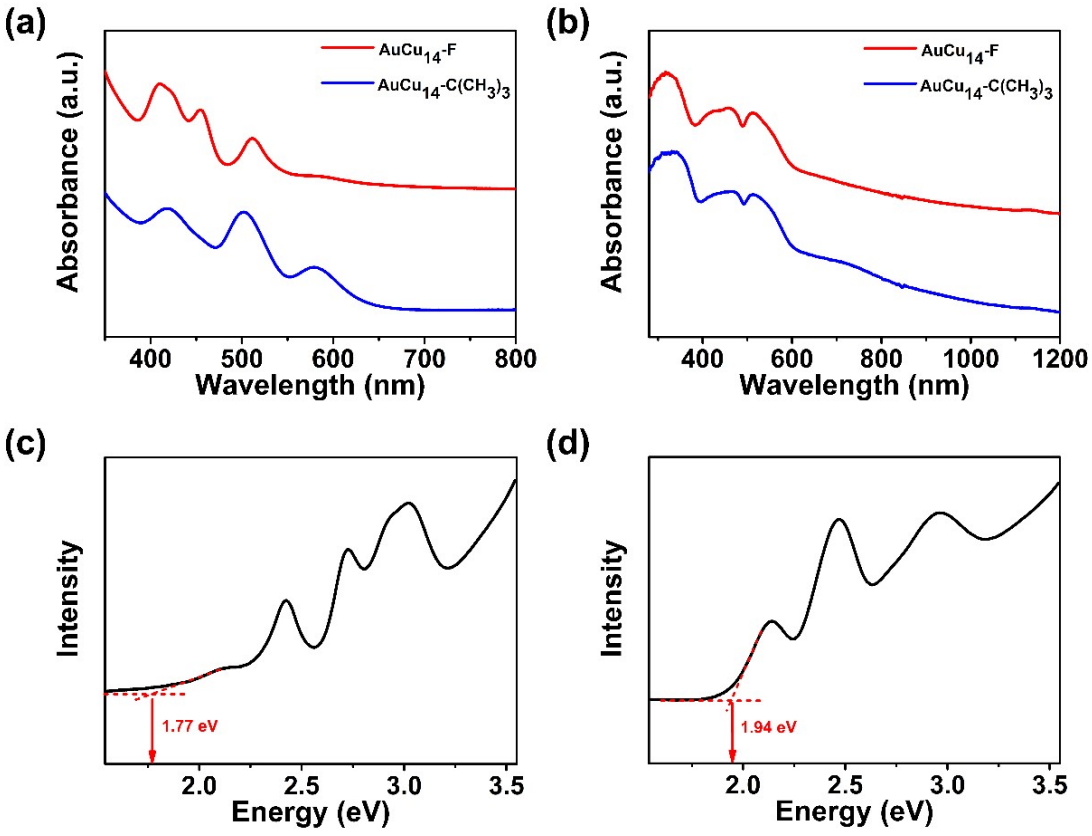

Fig. S8. (a) The UV-Vis absorption spectra of **$AuCu_{14}$-F** and **$AuCu_{14}$-$C(CH_3)_3$** in DCM. (b) UV-vis absorption of **$AuCu_{14}$-F** and **$AuCu_{14}$-$C(CH_3)_3$** solid. Optical gap determination of (c) **$AuCu_{14}$-F** and (d) **$AuCu_{14}$-$C(CH_3)_3$** in DCM.

Tab. S6. The Hirshfeld charge of single metal atom and the average Hirshfeld charge in each layer based on the optimized geometry of **$AuCu_{14}$-F** and **$AuCu_{14}$-$C(CH_3)_3$**. $Cu_{Cu\text{-}S}$ and Cu_{shell} refer to Cu atoms in the surface Cu-S motif and the Cu_8 shell.

$AuCu_{14}$-F		**$AuCu_{14}$-$C(CH_3)_3$**	
Atom	Hirshfeld Charge (e)	Atom	Hirshfeld Charge (e)
Au1	-0.106	Au1	-0.107
Cu1	0.177	Cu1	0.171
Cu2	0.177	Cu2	0.141
Cu3	0.145	Cu3	0.173
Cu4	0.145	Cu4	0.130
Cu5	0.130	Cu5	0.141
Cu6	0.177	Cu6	0.144
Cu7	0.145	Cu7	0.173
Cu8	0.177	Cu8	0.171
Cu9	0.177	Cu9	0.141
Cu10	0.145	Cu10	0.173
Cu11	0.145	Cu11	0.130
Cu12	0.130	Cu12	0.141
Cu13	0.177	Cu13	0.144
Cu14	0.145	Cu14	0.173
S1	-0.174	S1	-0.184
S2	-0.179	S2	-0.182
S3	-0.175	S3	-0.184
S4	-0.179	S4	-0.185
S5	-0.179	S5	-0.182
S6	-0.175	S6	-0.185
S7	-0.174	S7	-0.184
S8	-0.179	S8	-0.182
S9	-0.175	S9	-0.184
S10	-0.179	S10	-0.185
S11	-0.179	S11	-0.182
S12	-0.175	S12	-0.185

Average Hirshfeld Charge (e)				
	$Cu_{Cu\text{-}S}$	S	Cu_{shell}	Au
$AuCu_{14}$-F	0.177	-0.177	0.141	-0.106
$AuCu_{14}$-$C(CH_3)_3$	0.173	-0.183	0.139	-0.107

Tab. S7. Hirshfeld percentage of orbital compositions of frontier molecular orbitals in **$AuCu_{14}$-F** and **$AuCu_{14}$-$C(CH_3)_3$**.

		Au	Cu_8 shell	surface motifs
Compound	Orb#	Composition	Composition	Composition
$AuCu_{14}$-F	HOMO	16.64%	42.15%	41.21%
	LUMO	14.58%	34.87%	50.55%
$AuCu_{14}$-$C(CH_3)_3$	HOMO	17.28%	42.49%	40.23%
	LUMO	15.00%	34.53%	50.47%

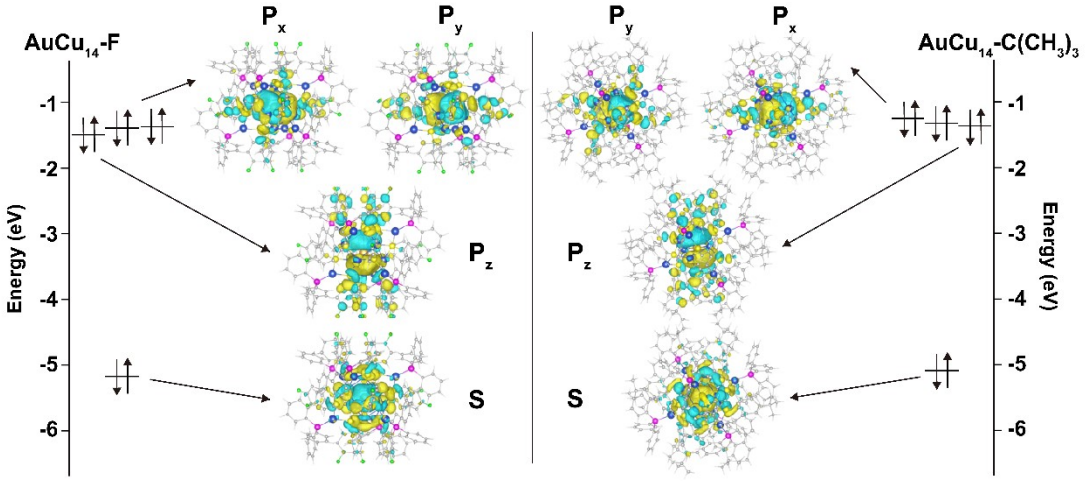

Fig. S9. Relative energy levels of frontier molecular orbitals of **$AuCu_{14}$-F** and **$AuCu_{14}$-$C(CH_3)_3$**.

Tab. S8. Emission quantum yield of **$AuCu_{14}$-F** and **$AuCu_{14}$-$C(CH_3)_3$** in CH_2Cl_2 ($c = 5\times10^{-5}$ mol/L) and solid state.

	λ_{max} (CH_2Cl_2)	Φ (CH_2Cl_2)	λ_{max} (solid)	Φ (solid)
$AuCu_{14}$-F	628 nm	3.81%	625 nm	27.14%
$AuCu_{14}$-$C(CH_3)_3$	747 nm	4.17%	650 nm	32.84%

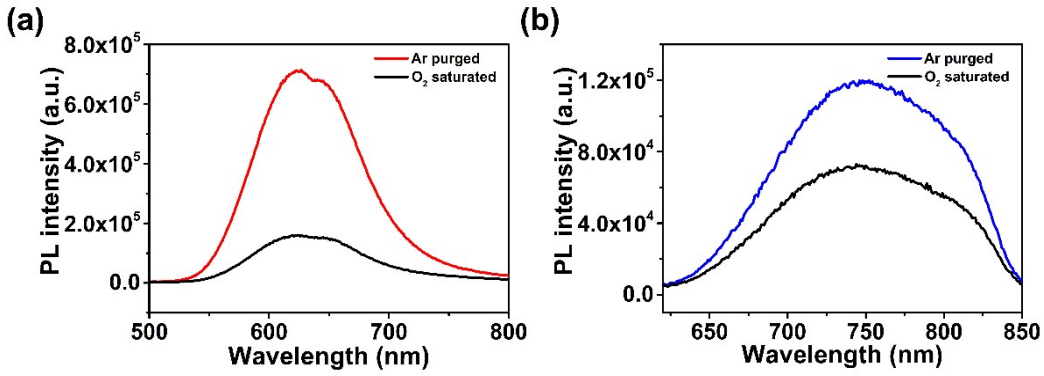

Fig. S10. The emission spectra of (a) **$AuCu_{14}$-F** and (b) **$AuCu_{14}$-$C(CH_3)_3$** in DCM under Ar-purged, O_2-saturated, **$AuCu_{14}$-F**: λ_{ex} = 408 nm; **$AuCu_{14}$-$C(CH_3)_3$**: λ_{ex} = 415 nm.

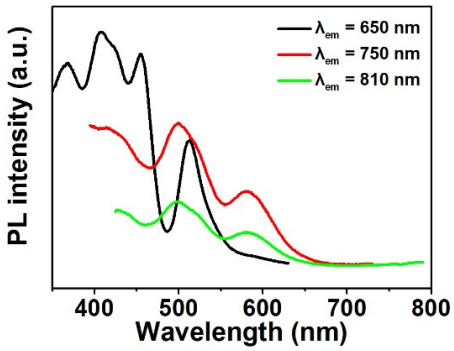

Fig. S11. The excitation spectra of **AuCu$_{14}$-F** in DCM with different emission wavelengths (650, 750 and 810 nm).

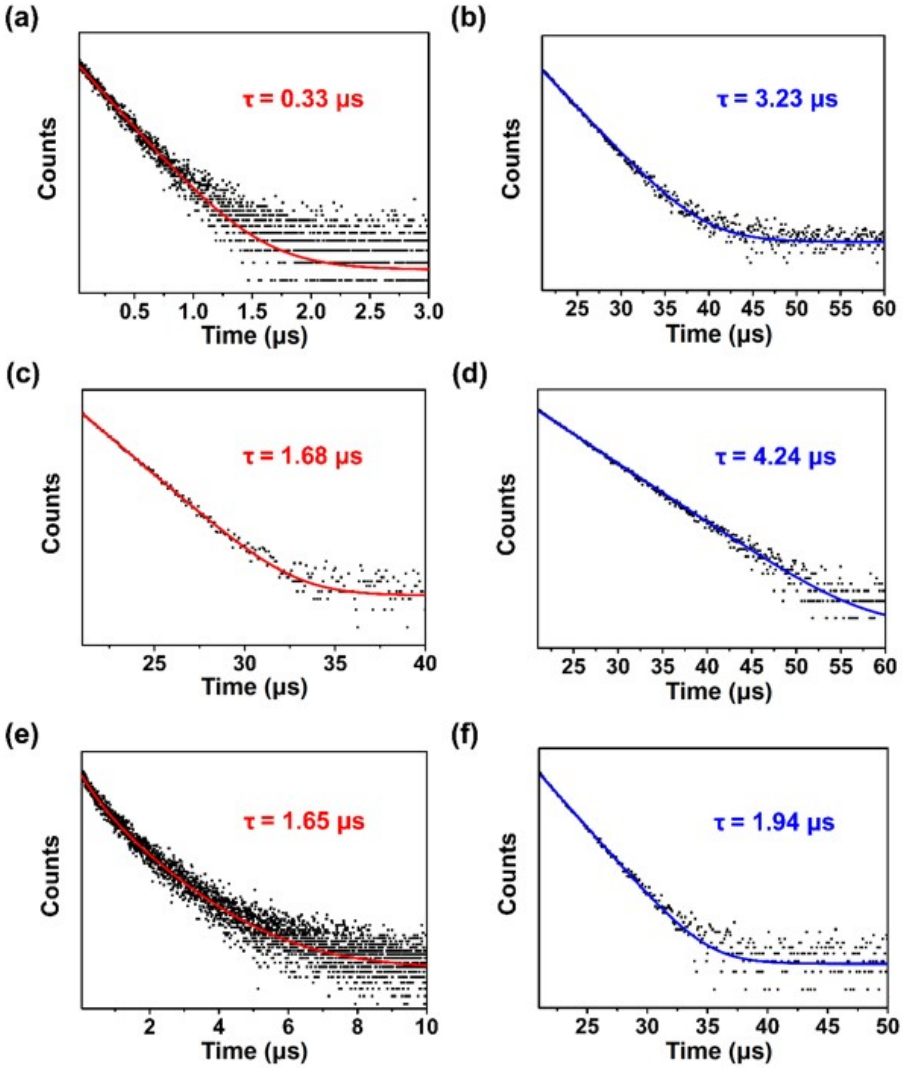

Fig. S12. RT time-resolved emission decays spectra of (a) **AuCu$_{14}$-F** in DCM at 628 nm, (b) **AuCu$_{14}$-C(CH$_3$)$_3$** in DCM at 747 nm, (c) **AuCu$_{14}$-F** in DCM under Ar-purged at 628 nm and (d) **AuCu$_{14}$-C(CH$_3$)$_3$** in DCM under Ar-purged at 747 nm, (e) **AuCu$_{14}$-F** crystal at 625 nm, (f) **AuCu$_{14}$-C(CH$_3$)$_3$** crystal at 650 nm.

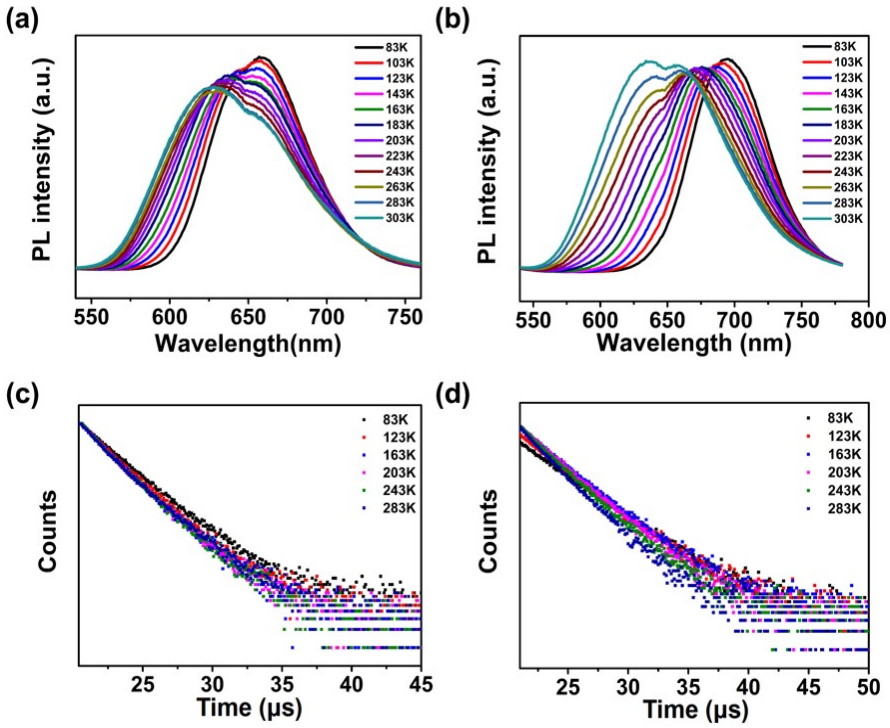

Fig. S13. The temperature-dependent emission spectra of (a) **AuCu$_{14}$-F** and (b) **AuCu$_{14}$-C(CH$_3$)$_3$** in the range of 83 to 303 K. The temperature-dependent emission decays spectra of (c) **AuCu$_{14}$-F** at 627 nm and (d) **AuCu$_{14}$-C(CH$_3$)$_3$** at 655 nm.

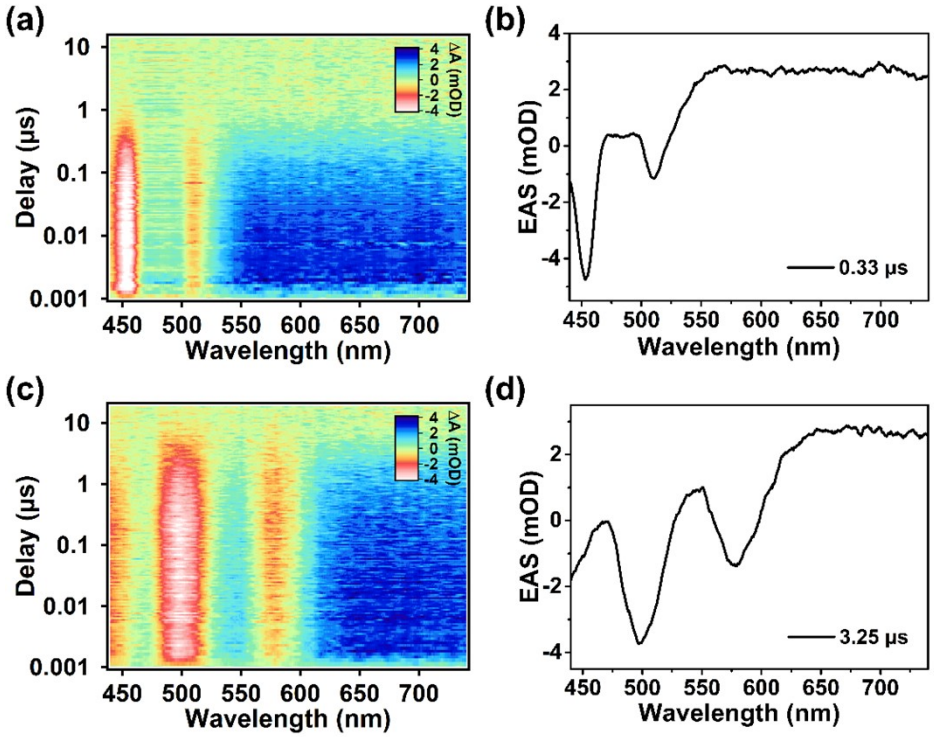

Fig. S14. The ns-TA data of (a) **AuCu$_{14}$-F** and (c) **AuCu$_{14}$-C(CH$_3$)$_3$** in DCM pumped at 400 nm. Evolution associated spectra (EAS) obtained from global analysis on the TA data of (b) **AuCu$_{14}$-F** and (d) **AuCu$_{14}$-C(CH$_3$)$_3$**.

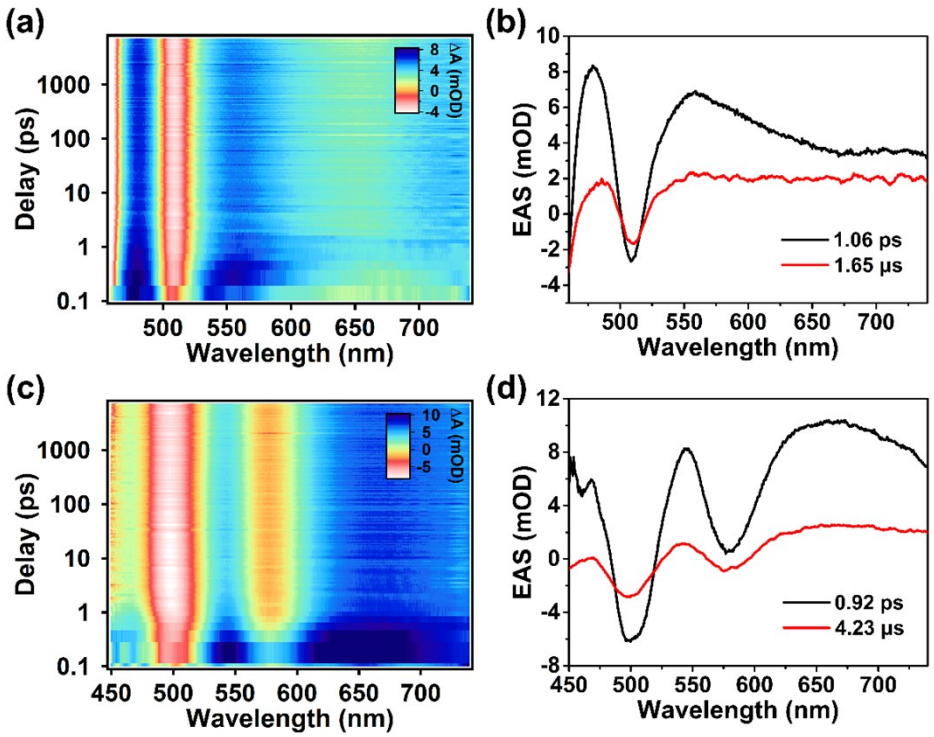

Fig. S15. The fs-TA data of (a) **AuCu$_{14}$-F** and (c) **AuCu$_{14}$-C(CH$_3$)$_3$** in DCM under Ar-purged pumped at 400 nm. Evolution associated spectra (EAS) obtained from global analysis on the TA data of (b) **AuCu$_{14}$-F** and (d) **AuCu$_{14}$-C(CH$_3$)$_3$**.

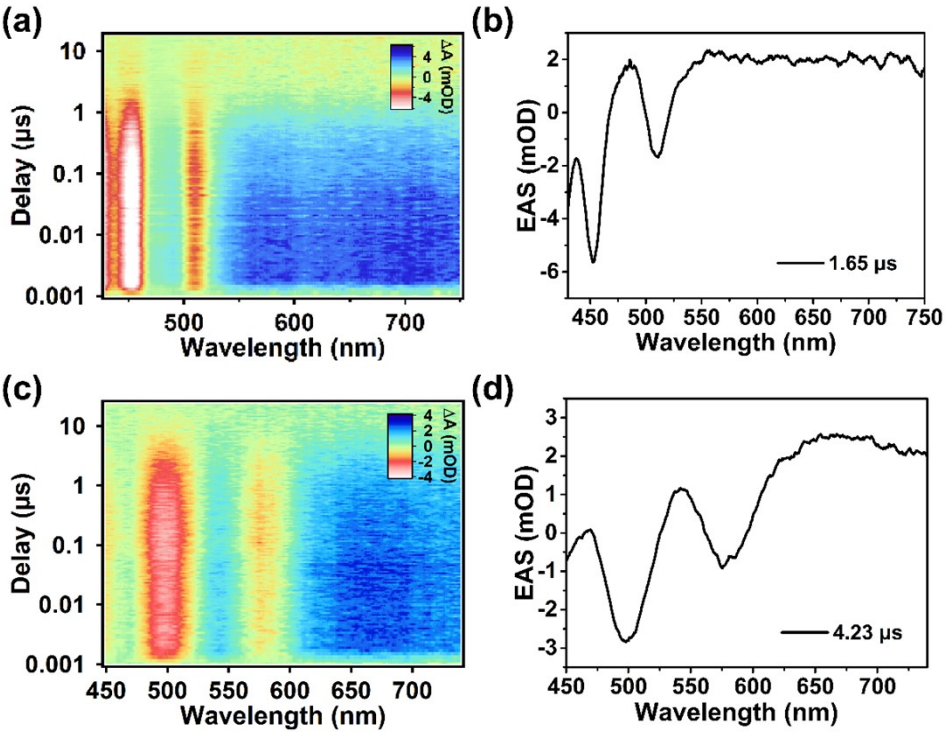

Fig. S16. The ns-TA data of (a) **AuCu$_{14}$-F** and (c) **AuCu$_{14}$-C(CH$_3$)$_3$** in DCM under Ar-purged pumped at 400 nm. Evolution associated spectra (EAS) obtained from global analysis on the TA data of (b) **AuCu$_{14}$-F** and (d) **AuCu$_{14}$-C(CH$_3$)$_3$**.

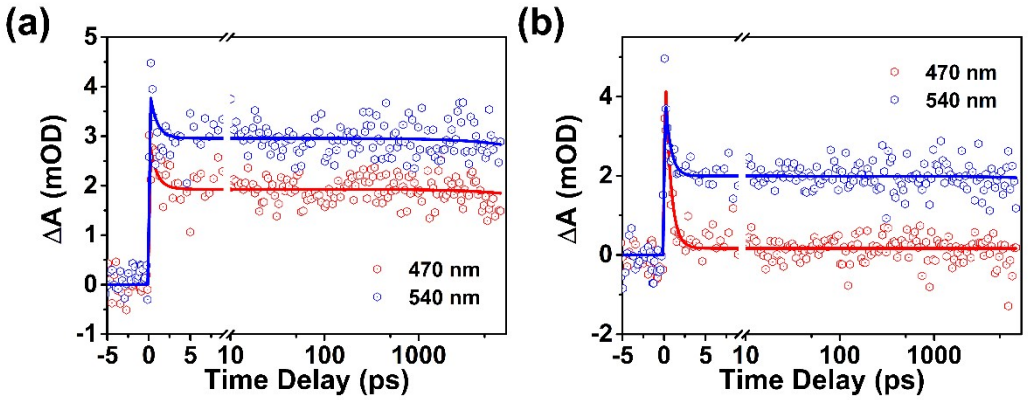

Fig. S17. The corresponding fitting kinetic traces at different wavelengths were obtained from global fitting for (a) **$AuCu_{14}$-F** and (b) **$AuCu_{14}$-$C(CH_3)_3$**.

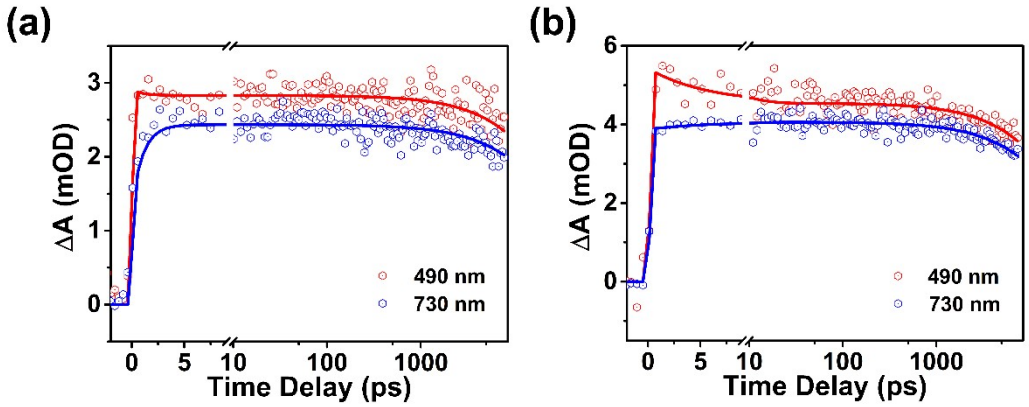

Fig. S18. The corresponding fitting kinetic traces at different wavelengths were obtained from global fitting for (c) **$AuCu_{14}$-F** and (d) **$AuCu_{14}$-$C(CH_3)_3$**.

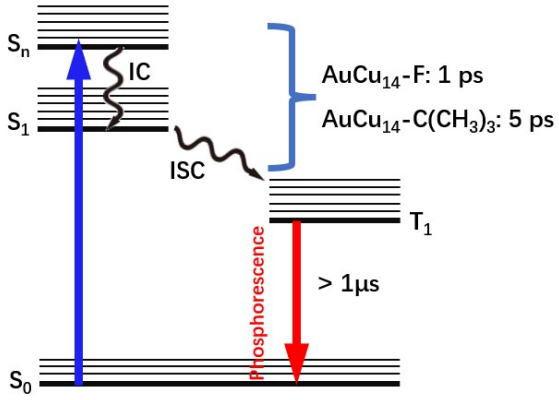

Fig. S19. Schematic diagram showing the excited-state relaxation dynamics of $AuCu_{14}$ in crystalline state.

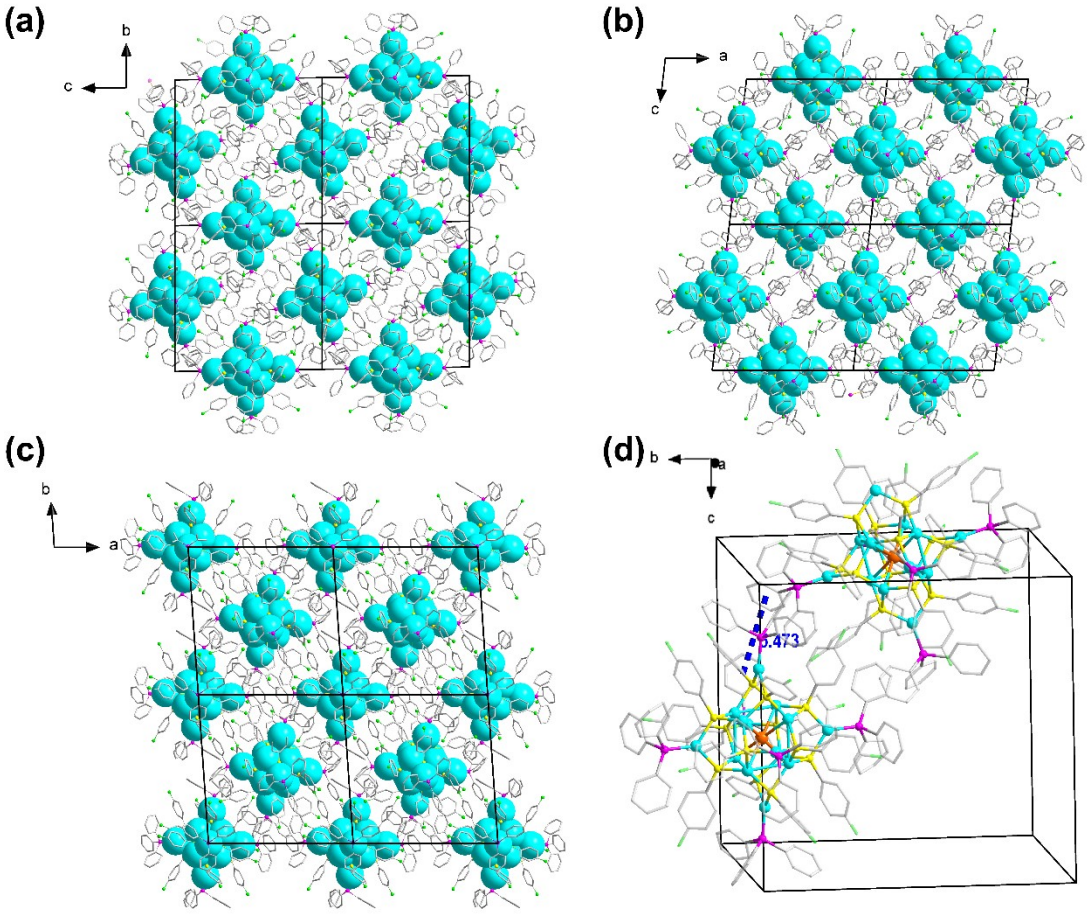

Fig. S20. Packing structure of **$AuCu_{14}$-F** in a 2 × 2 × 2 cell viewed along the (a) a, (b) b and (c) c axis. (d) Edge to face aromatic interactions between two adjacent **$AuCu_{14}$-F** molecules.[4, 5] Orange: Au, cyan: Cu, yellow: S, pink: P, gray: C, green: F. All hydrogen atoms have been omitted for clarity.

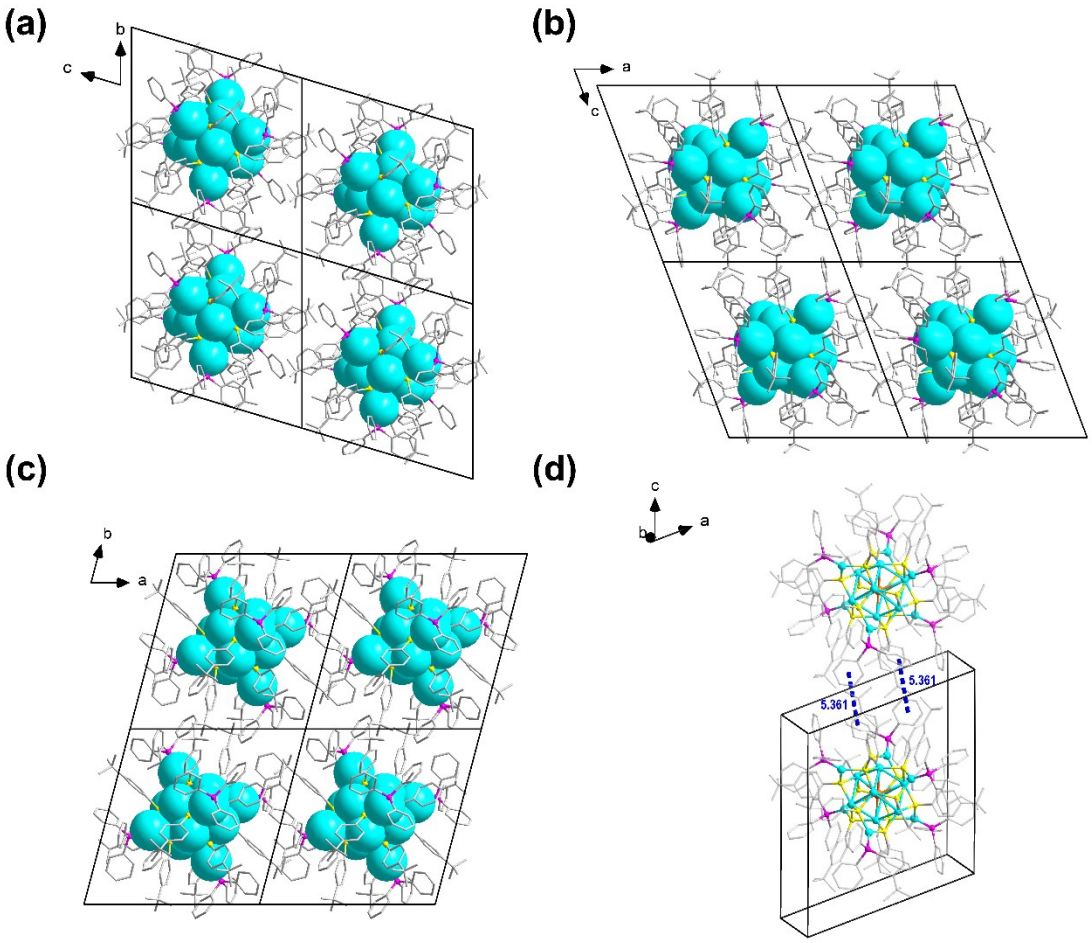

Fig. S21. Packing structure of **$AuCu_{14}$-$C(CH_3)_3$** in a 2 × 2 × 2 cell viewed along the (a) a, (b) b and (c) c axis. (d) Edge to face aromatic interactions between two adjacent **$AuCu_{14}$-$C(CH_3)_3$** molecules.[4, 5] Orange: Au, cyan: Cu, yellow: S, pink: P, gray: C. All hydrogen atoms have been omitted for clarity.

Supplementary References

1 H. Shen, Y. Z. Han, Q. Wu, J. Peng, B. K. Teo and N. Zheng, *Small Methods*, 2020, **5**, 2000603.

2 H. Li, F. Song, D. Zhu, Y. Song, C. Zhou, F. Ke, L. Lu, X. Kang and M. Zhu, *Journal of the American Chemical Society*, 2022, **144**, 4845-4852.

3 M. J. Frisch, G. W. Trucks, H. B. Schlegel, G. E. Scuseria, M. A. Robb, J. R. Cheeseman, G. Scalmani, V. Barone, G. A. Petersson, H. Nakatsuji, X. Li, M. Caricato, A. V. Marenich, J. Bloino, B. G. Janesko, R. Gomperts, B. Mennucci, H. P. Hratchian, J. V. Ortiz, A. F. Izmaylov, J. L. Sonnenberg, Williams, F. Ding, F. Lipparini, F. Egidi, J. Goings, B. Peng, A. Petrone, T. Henderson, D. Ranasinghe, V. G. Zakrzewski, J. Gao, N. Rega, G. Zheng, W. Liang, M. Hada, M. Ehara, K. Toyota, R. Fukuda, J. Hasegawa, M. Ishida, T. Nakajima, Y. Honda, O. Kitao, H. Nakai, T. Vreven, K. Throssell, J. A. Montgomery Jr., J. E. Peralta, F. Ogliaro, M. J. Bearpark, J. J. Heyd, E. N. Brothers, K. N. Kudin, V. N. Staroverov, T. A. Keith, R. Kobayashi, J. Normand, K. Raghavachari, A. P. Rendell, J. C. Burant, S. S. Iyengar, J. Tomasi, M. Cossi, J. M. Millam, M. Klene, C. Adamo, R. Cammi, J. W. Ochterski, R. L. Martin, K. Morokuma, O. Farkas, J. B. Foresman and D. J. Fox, *Journal*, 2016.

4 S. K. Burley and G. A. Petsko, *Science*, 1985, **229**, 23-28.

5 L. He, Z. Gan, N. Xia, L. Liao and Z. Wu, *Angewandte Chemie International Edition*, 2019, **58**, 9897-9901.